e-ISSN: 2687-6698 **Research Article**

Turkish Journal of

Analytical Chemistry

TurkJAC

https://dergipark.org.tr/tr/pub/turkjac

Magnetic biochar derived from olive pomace for efficient tetracycline removal from water

Burcu Kabak

Burdur Mehmet Akif Ersoy University, Faculty of Arts and Science, Chemistry Department, 15100, Burdur, Türkiye

Abstract

The uncontrolled release of tetracycline (TC), a widely used antibiotic, poses a significant threat to aquatic ecosystems owing to its persistence and contribution to antibiotic resistance. In this study, magnetic biochar (MOBC) derived from olive pomace was synthesised and characterised by FTIR, XRD, BET, TGA, and FESEM-EDX. The specific surface area increased from 0.87 to 37.41 m^2/g and the total pore volume increased from 0.0038 to 0.1341 cm^3/g after magnetic functionalization. The MOBC exhibited a high adsorption capacity of 248.77 mg/g at 25 °C, reaching equilibrium within 100 min. The adsorption followed pseudo-first-order kinetics and Langmuir isotherm, with thermodynamic analysis indicating a spontaneous ($\Delta G°$ = –17.83 to –19.70 kJ/mol) and exothermic ($\Delta H°$ = –3.74 kJ/mol) process. The desorption efficiency reached 87% using 2 M NaOH, and the MOBC maintained >90% removal efficiency in real water samples at a dosage of 2 g/L. These findings highlight a novel and practical approach for valorising agricultural waste through magnetic biochar functionalization, offering a strong potential for sustainable water treatment applications.

Keywords: Biochar, olive pomace, tetracycline removal, magnetic functionalization, water treatment, adsorption

1. Introduction

The increasing prevalence of pharmaceutical contaminants, particularly antibiotics such as tetracycline, in aquatic ecosystems has become a pressing global environmental issue. Tetracycline is frequently detected in surface and groundwater sources, and often results from agricultural runoff, improper disposal methods, and pharmaceutical wastewater discharge [1–6]. This presents significant challenges owing to its persistent nature and potential to foster antibiotic resistance in bacterial populations, necessitating innovative approaches for its effective removal from water sources [7].

Traditional methods for tetracycline removal, including chemical oxidation, membrane filtration, and biological treatments, often fall short of efficacy and produce secondary pollutants as byproducts [8]. These limitations have fuelled interest in adsorption processes, which are recognised for their simplicity, efficiency, and low operational costs. Biochar resulting from the pyrolysis of biomass has emerged as a promising adsorbent owing to its high surface area, porous structure, and functional groups, which are conducive to adsorbing organic pollutants such as tetracycline [9–12].

The use of agricultural wastes, such as olive pomace, for biochar production not only addresses the waste disposal issues inherent to the olive oil industry but also offers a proactive method to manage pharmaceutical contaminants in water [13,14]. Olive pomace is abundant and rich in organic matter, and its transformation into biochar enhances its functionality and usability in water treatment applications [15,16]. Olive oil production generates significant amounts of mill waste, particularly olive pomace, which is composed of lignin, cellulose, and residual oil. The annual production of olive oil is approximately 3 million tons, leading to approximately 12 million tons of olive pomace, particularly in countries like Türkiye, which rank among the top producers of olive oil [17–19]. Olive pomace is traditionally used in low-value applications, such as animal feed, land spreading, and combustion for energy generation [20,21]. However, their extensive availability highlights the need for higher-value applications. Recent studies

Citation: B. Kabak, Magnetic biochar derived from olive pomace for efficient tetracycline removal from water, Turk J Anal Chem, 7(3), 2025, 268–281.

***Author of correspondence:** burcukabak@hotmail.com
Tel: +90 (286) 218 00 18 **Fax:** n/a
Received: May 15, 2025 **Accepted:** July 12, 2025
https://doi.org/10.51435/turkjac.1699857

have focused on the valorization of olive pomace through thermochemical conversion into value-added materials, including biochar, activated carbon, and bioplastics. These materials are gaining traction because of their potential applications in wastewater treatment, soil enhancement, and industrial sorbents [22–24]. Such transformations not only reduce the environmental burden associated with olive pomace disposal but also contribute to economic benefits by providing functional materials aligned with circular economy principles [25]. The commitment to transforming olive pomace from waste into a resource underscores a significant shift towards sustainability in the olive oil industry, maximising the value obtained from each ton of processed olives.

Although olive pomace-derived biochar shows great potential for sustainable application, its unmodified form often lacks sufficient functional properties for high-performance pollutant removal. The challenge with unmodified biochar, however, lies in its often-inadequate adsorption capacity due to limited surface functionalities, which diminishes its effectiveness against organic contaminants, such as tetracycline [26]. To enhance the performance of biochar, methods for its functionalization have been explored, notably magnetic modification, which not only increases the adsorption efficiency but also facilitates the removal of biochar from polluted water through magnetic separation techniques [27]. This approach is particularly advantageous for large-scale applications, as it presents a sustainable and cost-effective solution for wastewater treatment.

Recent studies have explored the use of biochar derived from various biomass sources, such as lignin-rich residues [28], olive mill waste [29], and other lignocellulosic feedstocks [30], for the removal of pharmaceutical contaminants including tetracycline (TC). These adsorbents demonstrate promising removal efficiencies, but often suffer from limited surface area, insufficient regeneration performance, or the requirement of costly activation techniques (e.g. Zn/Fe chemical activation) [31]. Although biochar has been recognised as a sustainable material for TC removal, its effectiveness depends heavily on the feedstock and the modification strategy [32]. In contrast to previous studies, the present study introduces magnetically functionalized biochar synthesised from olive pomace, a widely available agro-industrial waste. The resulting material exhibited a remarkably high surface area (37.41 m^2/g), superior adsorption capacity (248.77 mg/g), and excellent regeneration ability (87% desorption efficiency with 2 M NaOH), all achieved without the use of metal impregnation. This novel approach not only valorises agricultural waste in line with circular economy principles but also provides a cost-effective and environmentally friendly alternative for the efficient removal of TC from water.

2. Materials and methods

2.1. Materials

Tetracycline (98%), $FeSO_4 \cdot 7H_2O$, $FeCl_3 \cdot 6H_2O$, sodium hydroxide (≥98%), sodium chloride (99%), hydrochloric acid (37%), methyl alcohol (≥99.9%), acetonitrile (99%), ethyl alcohol (≥99%) were obtained from Sigma Aldrich and utilised without additional purification.

2.2. Preparation of biochar (OBC)

Olive pulp was obtained from various local olive oil producers in the Fethiye region of Muğla Province (Turkey), air-dried at room temperature for one week, and homogenized before pyrolysis. The dried material was ground into a fine powder (0.16–0.25 mm) using a ball mill. Approximately 40 g of the powder was placed in a closed porcelain crucible and pyrolyzed in a muffle furnace (Protherm PLF 120/10) under oxygen-limited conditions. The temperature was increased to 400 °C at a rate of 10 °C/min and held for 4 h to ensure carbonization. After natural cooling (~24 h), the obtained biochar was washed with deionised water until the pH was neutral, dried at 80 °C, and designated as OBC.

2.3. Magnetic functionalization

Magnetic biochar was synthesised by applying minor modifications of the co-precipitation methods reported in the literature [33,34]. As an iron source, 8 g of $FeSO_4 \cdot 7H_2O$ and 12 g and $FeCl_3 \cdot 6H_2O$ were weighed at a mass ratio of 1:1.5 and dissolved in 100 mL of deionized water to prepare an aqueous solution. The pH of the solution was adjusted to 10 using 0.10 M NaOH. Subsequently, 10 g of OBC was placed in a three-necked flask and an iron solution was added. The mixture was stirred at 70 °C under nitrogen atmosphere for 1 h. After the reaction, the mixture was filtered and the solid residue remaining on the filter paper was washed with deionized water until a neutral pH was achieved. The magnetic biochar was dried in an oven at 80 °C for 24 h. The resulting magnetic biochar was labelled MOBC. The successful magnetic functionalization of the biochar is also visually demonstrated in the Supporting Information (Fig. S1), where the MOBC sample was attracted by an external magnet while the OBC remained unaffected, indicating the presence of magnetic components only in the modified biochar.

2.4. Characterization of biochar

The synthesized adsorbents were characterized using various analytical techniques to evaluate their structural, morphological, surface area, and chemical properties.

The surface morphology and chemical composition of the biochar derived from olive pulp waste biomass and the modified biochar were examined using Field Emission Scanning Electron Microscopy (FESEM) (Zeiss, Model: ULTRA Plus) coupled with Energy Dispersive X-ray Spectroscopy (EDX). The functional groups present on the biochar surface were identified using Fourier Transform Infrared (FTIR) spectroscopy (Shimadzu, Model: Affinity-1S) over a frequency range of 400–4000 cm^{-1}. Structural analysis of the biochar was performed using Powder X-ray Diffraction (P-XRD) (PANalytical, Model: Empyrean) in the 2θ range 10–90°. The specific surface area, pore size, and pore volume of the biochar and modified biochar were determined using Brunauer–Emmett–Teller (BET) analysis. This analysis provided critical information on the adsorption capacities of the adsorbents. Additionally, the thermal behaviour and biomass characteristics of the biochar were evaluated using Thermogravimetric Analysis (TGA) (PerkinElmer, Model: TGA 4000). The point of zero charge (PZC) of OBC and MOBC was determined using the conventional drift method [2]. For this measurement, approximately 50 mg of biochar sample was dispersed in 25 mL of 0.1 M NaCl solution. The initial pH of the solution was adjusted between 2.0 and 12 by gradual addition of either 1 M NaOH or 1 M HCl. The suspensions were placed on a shaker and maintained at 25 °C for 24 h. Following this, the final pH values were measured using a pH meter (Orion 3 Star, Thermo Scientific).

2.5. Adsorption experiments

The adsorption capacities of OBC and MOBC for tetracycline (TC) ions at room temperature were investigated using a batch technique. All working solutions were prepared from TC stock solutions at a concentration of 1000 mg/L. To determine the optimal conditions for the maximum adsorption capacity, various parameters were examined, including the initial solution pH, adsorbent dosage, contact time, initial solution concentration, and temperature. The pH of the solutions was adjusted to 2.0 to 12.0 using 0.1 M NaOH and 0.1 M HCl solutions. Adsorption experiments were conducted with adsorbent dosages ranging from 0.5 g/L to 2 g/L, at different contact times between 0 and 240 min, with initial TC concentrations ranging from 5 to 800 mg/L, and at three different temperatures (25, 45, and 65 °C). The initial and final TC concentrations were measured at a wavelength of 365 nm using a UV-Vis spectrophotometer (PG Instruments, Model T60). Three replicates were used for each measurement and the average values were calculated. To evaluate the desorption efficiency of the adsorbent, experiments were conducted using samples obtained under the optimal adsorption conditions (20 mg/L TC, 2 g/L MOBC, pH 6.0, and 25 °C). After the adsorption process, the solution was filtered and the MOBC adsorbent was washed with deionized water and dried at 70 °C overnight. Different desorption agents, including acetonitrile (ACN), ethanol, methanol, 0.5 M HCl, and 0.5–2 M NaOH, were tested to desorb TC from the MOBC surface.

2.6. Adsorption of kinetics and isotherms

The adsorption kinetics were evaluated using experimental data collected at various contact times by applying four different models: pseudo-first-order (PFO), pseudo-second-order (PSO), Elovich, and intra-particle diffusion (IPD). To describe the equilibrium adsorption behaviour, isotherm analyses were conducted using datasets within a concentration range of 5–800 mg/L across three temperatures (25 °C, 45 °C, and 65 °C). The experimental results were interpreted using commonly used isotherm models, including the Langmuir, Freundlich, Redlich–Peterson, Sips, and Toth equations. Microsoft Excel and OriginPro 2025 were used to perform the initial data screening and create visual representations, respectively. In addition, OriginPro 2025 was used to fit the kinetic and isotherm models. The experiments were conducted in triplicate, and the results are presented as the mean value ± standard deviation (SD). Further details regarding the mathematical formulations and fitting parameters of the kinetic and isotherm models are provided in Supplementary Section 1.

3. Results and discussion

3.1. Characterization results

Fourier Transform Infrared (FTIR) spectroscopy was employed to identify the surface functional groups of OBC and MOBC (Fig. 1a). The broad band around 3429 cm^{-1} in both samples corresponds to –OH stretching vibrations from alcohols, phenols, and carboxylic acids, which enhance the hydrogen bonding and adsorption capacity [35,36]. The peaks at 2916 and 2848 cm^{-1} are attributed to aliphatic $–CH_2$ and $–CH_3$ groups, respectively, with higher intensity in OBC, indicating a greater presence of aliphatic structures [37]. Variations in the FTIR peak intensity align with the biomass source and treatment conditions [38]. The band at 1558 cm^{-1} indicates carbonyl (C=O) and carboxyl (–COOH) groups, which contribute to surface multifunctionality [39]. A distinct peak at ~574 cm^{-1} in MOBC confirms Fe–O stretching, indicating successful iron oxide incorporation [40–43].

The broad and irregular peak observed in the OBC sample between 20° and 30° (Fig. 1b) indicates an amorphous carbon structure, which is typical of biochar produced via high-temperature pyrolysis [44].

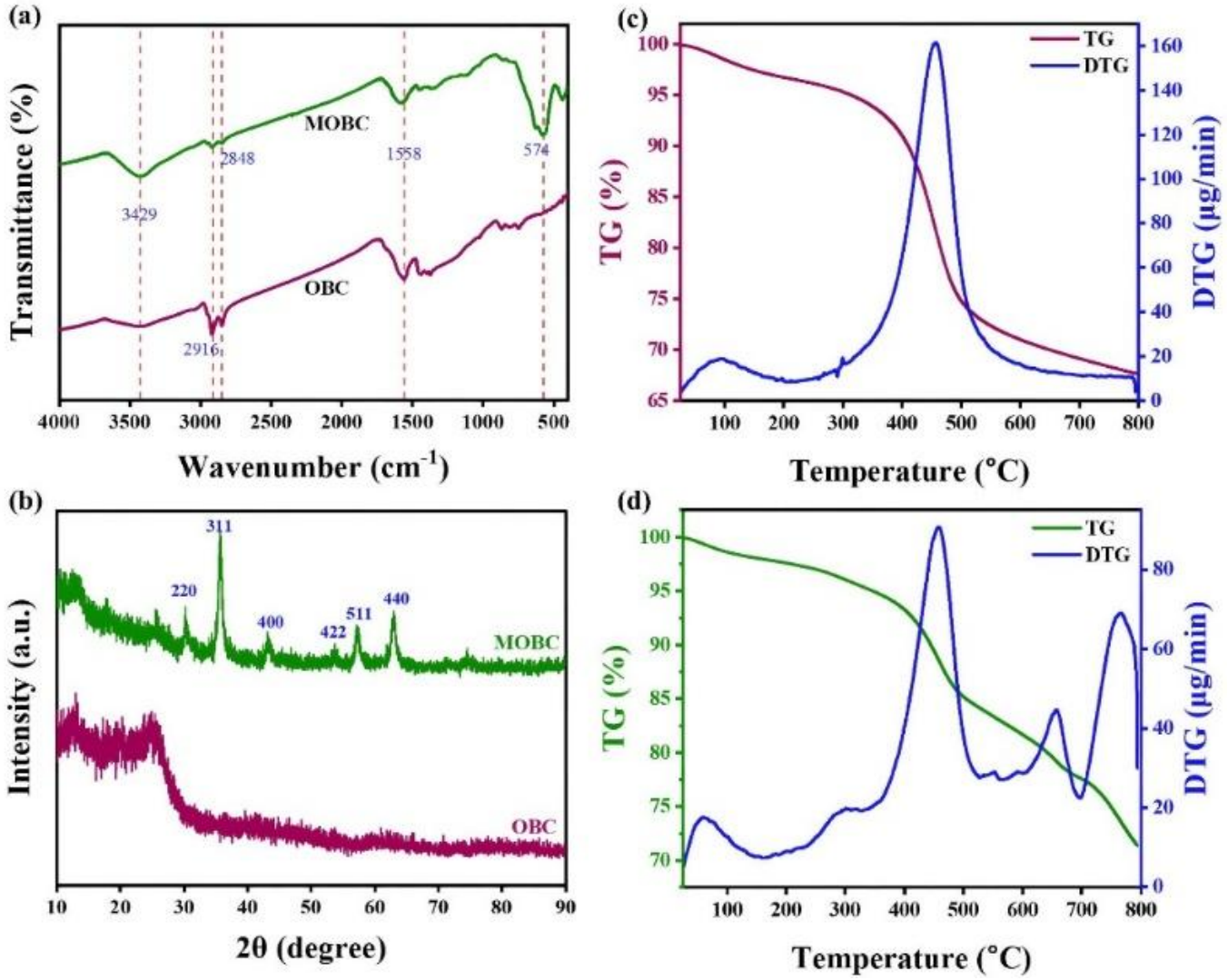

Figure 1. (a) FTIR spectra of OBC and MOBC, (b) XRD pattern of OBC and MOBC, (c) TGA curve of OBC, (d) TGA curve of MOBC

This amorphous phase results from thermal transitions during carbonisation and is influenced by the heating profile [45,46]. In contrast, MOBC exhibits sharp and distinct peaks, particularly at 35.5°, corresponding to the (311) plane of magnetite (Fe_3O_4), confirming its crystalline nature. These peaks align with standard Fe_3O_4 patterns (COD card no. 9005812) and indicate successful magnetite formation within the carbon matrix [47,48]. The XRD results support the effective integration of iron-oxide phases into the biochar structure, enhancing its magnetic properties [49,50].

The TGA–DTG results for OBC (Fig. 1c) and MOBC (Fig. 1d) provide insights into their thermal stability and composition. Both materials showed an initial mass loss below 150 °C owing to moisture evaporation, which is typical for lignocellulosic biochar [51,52]. The main degradation occurred between 300 and 500 °C for OBC and slightly shifted to 350–500 °C for MOBC, corresponding to the breakdown of hemicellulose, cellulose, and lignin [53,54]. MOBC exhibited a more complex DTG pattern, including additional peaks between 600 and 750 °C, linked to transformations of iron oxide species (e.g., $Fe_3O_4 \rightarrow Fe_2O_3$ or Fe^0), absent in OBC [55]. The higher residual mass above 750 °C in the MOBC confirms the presence of thermally stable magnetic phases [56]. These findings highlight MOBC's enhanced thermal resistance and functional versatility due to magnetic modification, supporting its potential for adsorption and catalysis [57,58].

The surface morphologies of the OBC and MOBC samples were investigated using FESEM analysis. As shown in Fig. 2a and Fig. 2b, the pristine biochar (OBC) exhibited a relatively smooth and compact surface with limited pore development, which is indicative of its unmodified structure. In contrast, magnetic biochar (MOBC) demonstrated a rougher surface morphology with the presence of aggregated nanoparticles and visible mesopores, confirming successful magnetic functionalization.

These morphological changes contributed to increased surface heterogeneity and the formation of additional adsorption sites, enhancing the affinity of the material for tetracycline.

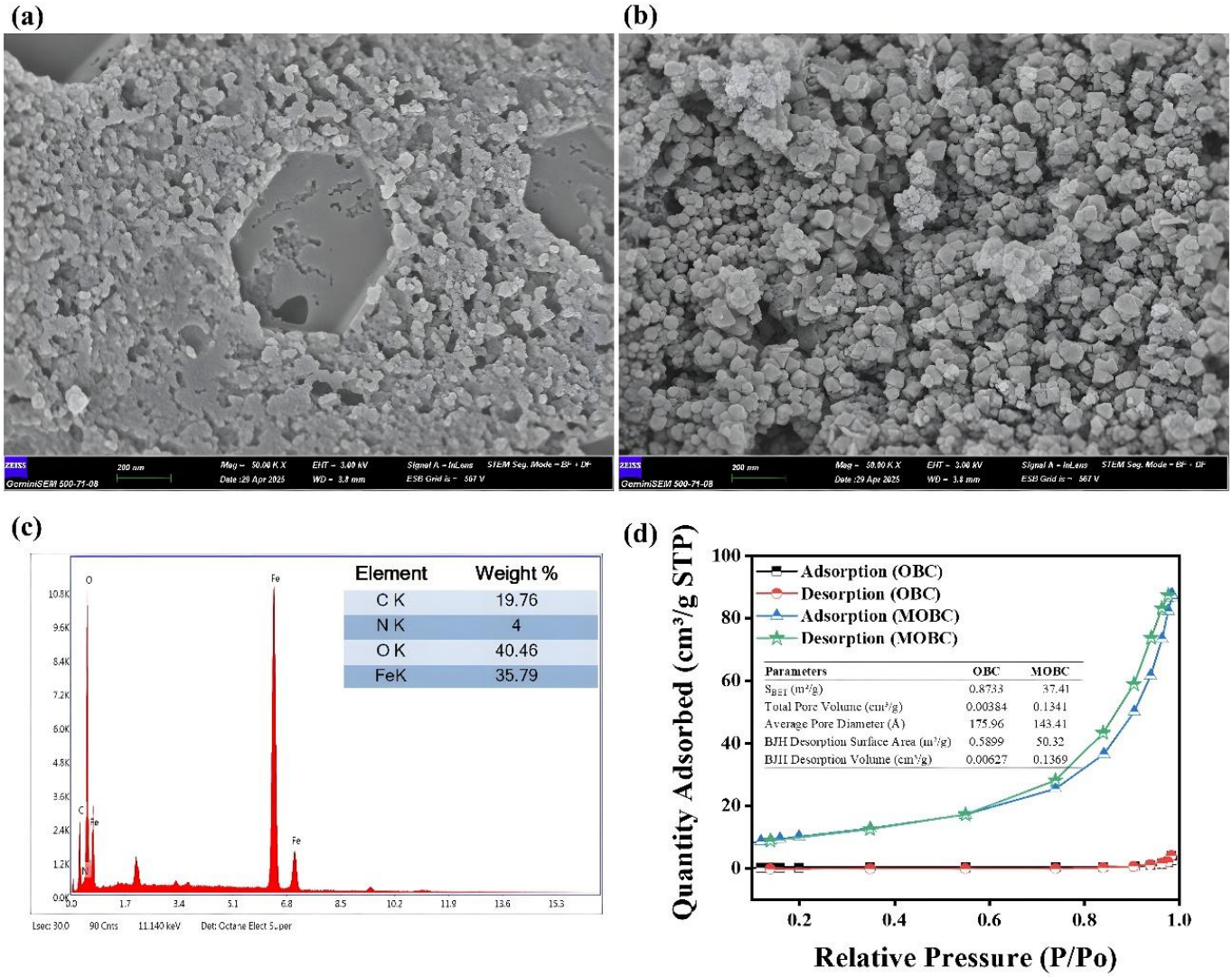

Figure 2. SEM images of (a) OBC, (b) MOBC, (c) EDX spectrum of MOBC, (d) N_2 adsorption–desorption isotherms of OBC and MOBC

This transformation is consistent with previous findings by Monteagudo et al. (2025) [59] and Alcazar-Ruiz et al. (2024) [60], where the activation of olive pomace-derived biochar via chemical (KOH) or physical (CO_2, steam) routes induced significant textural development. In their studies, the activation processes similarly led to greater surface irregularities and pore formation, which were linked to improved gas adsorption capacities. While our synthesis approach employed magnetic functionalization instead of classical chemical activation, the surface improvements observed in the SEM images are comparable to those obtained via KOH activation, as both approaches enhance active site accessibility.

Complementary EDX analysis confirmed the presence of iron (Fe) as a major component in MOBC, with a weight percentage of 35.79% (Fig. 2c), verifying successful functionalization with iron-based magnetic particles. Additionally, the elemental composition included oxygen (40.46 wt%), carbon (19.76 wt%), and nitrogen (4 wt%), suggesting the retention of oxygen-containing functional groups that may contribute to electrostatic interactions and π–π bonding with TC molecules. These morphological and compositional enhancements validated the improved adsorption capacity and magnetic recoverability of the MOBC adsorbent.

BET analysis revealed a marked improvement in the textural properties of biochar upon magnetic functionalization. The specific surface area increased from 0.8733 m^2/g for OBC to 37.41 m^2/g for MOBC, while the total pore volume expanded from 0.0038 to 0.1341 cm^3/g (Fig. 2d). This significant enhancement demonstrated the development of a mesoporous structure with improved diffusion paths and higher surface availability. Although the BET surface area of MOBC is lower than those reported for some chemically activated biochars (e.g. >900 m^2/g in CO_2/steam-activated biochars or >1000 m^2/g in KOH-activated samples) [59,60] it is important to note that our material was not subjected to harsh chemical treatment or high-temperature activation.

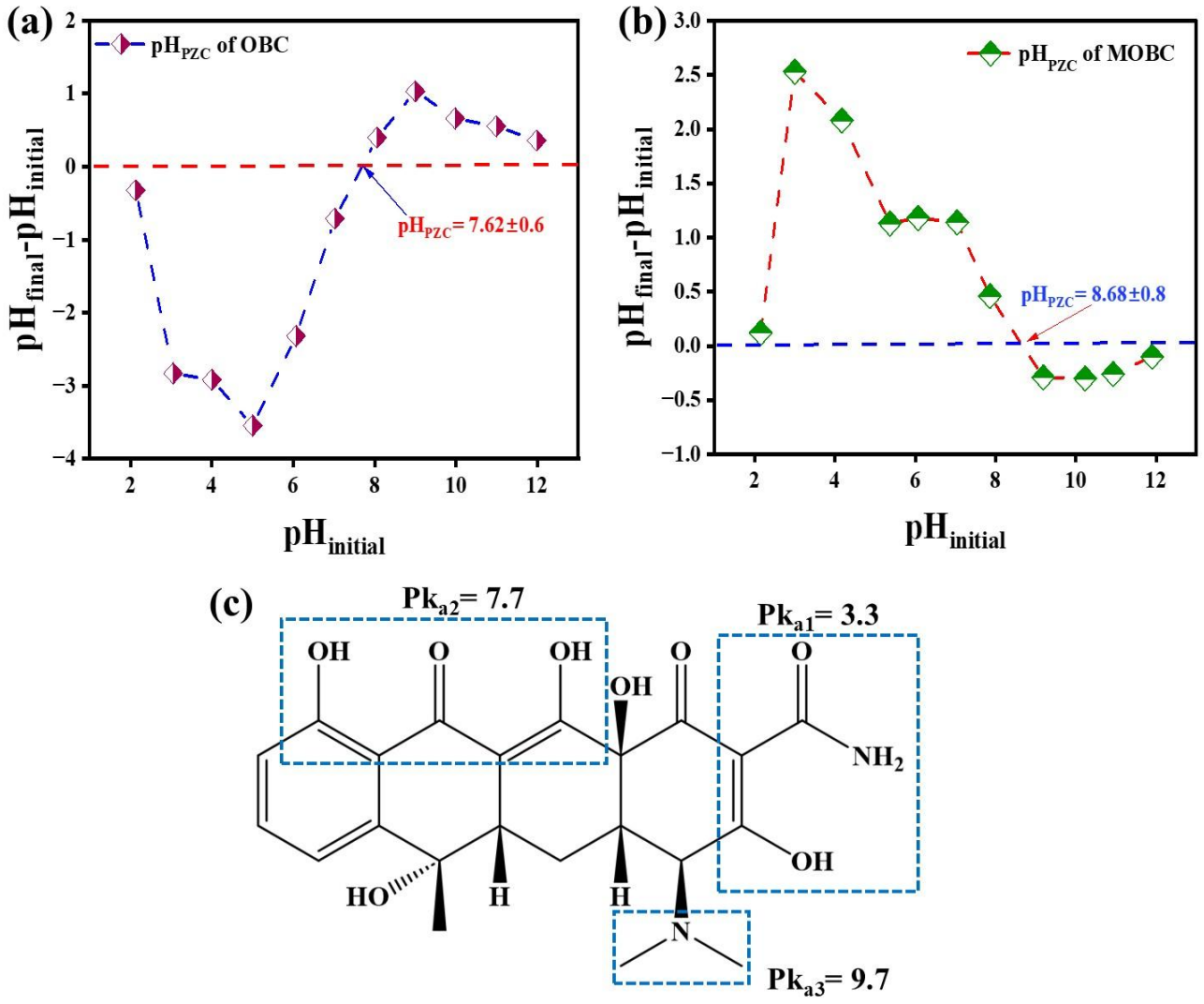

Figure 3. The pHpzc of (a) OBC, (b) MOBC, (c) TC structure

Instead, the observed increase in surface area and pore volume is attributed to the incorporation of magnetic particles, which created a moderately porous structure while preserving environmental compatibility and avoiding corrosive agents like KOH or H_3PO_4. This makes MOBC a promising, low-cost, and sustainable alternative, especially in applications where a moderate surface area combined with easy magnetic recovery is advantageous.

Additionally, nitrogen adsorption–desorption isotherms confirmed the mesoporous nature of the material. The MOBC sample exhibited a Type IV isotherm with a pronounced hysteresis loop, which is typical for mesoporous materials, whereas the OBC sample showed a Type III isotherm, suggesting minimal adsorption affinity. This transition aligns with the literature, where structural modifications such as pore widening or metal incorporation often shift the adsorption behaviour from low-capacity to mesoporous-dominated profiles [61,62].

In summary, SEM and BET characterisations support the successful synthesis of structurally enhanced, magnetically recoverable biochar with favourable textural properties. While the surface area remains modest compared to aggressively activated biochars, the balance between adsorption efficiency, cost-effectiveness, and magnetic separability provides MOBC with competitive advantages for environmental applications.

The point of zero charge (pHpzc) is a key parameter for understanding the electrostatic interactions between adsorbents and charged pollutants, such as TC. It defines the pH at which the adsorbent surface has a net zero charge: positively charged below and negatively charged above [2]. Fig. 3 illustrates the pHpzc values of OBC and MOBC. As shown in Fig. 3a, OBC exhibits a pHpzc of 7.62 ± 0.6, while MOBC shows a higher value (8.68 ± 0.8) (Fig. 3b), indicating that magnetic modification increases the surface basicity, likely due to iron oxide incorporation. This shift suggests that under neutral or slightly acidic conditions (pH < 7), MOBC maintains a positively charged surface across a broader pH range than OBC.

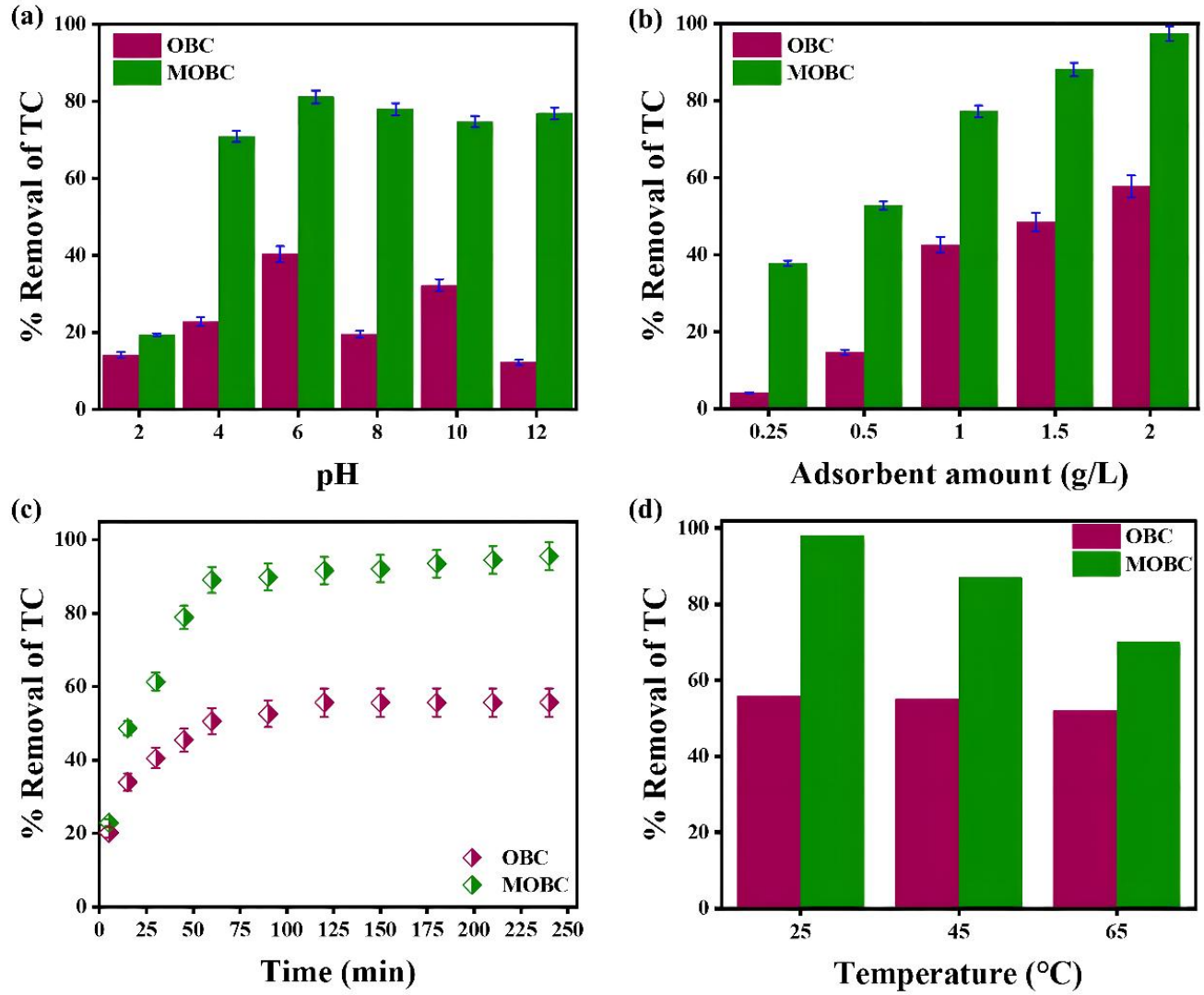

Figure 4. Optimization of (a) pH (adsorption conditions: 20 mg/L TC, 1 g/L adsorbent amount, 25 mL, 25 °C, 4h), (b) adsorbent amount (adsorption conditions: 20 mg/L TC, pH = 6.04, 25 mL, 25 °C, 4h), (c) time (adsorption conditions: 20 mg/L TC, 2 g/L adsorbent amount, pH = 6.04, 25 mL, 25 °C), (d) temperature (adsorption conditions: 20 mg/L TC, 2 g/L adsorbent amount, 25 mL, pH = 6.04, 2h).

This behaviour enhances electrostatic attraction with TC, which exists in anionic or zwitterionic forms depending on the pH (Fig. 3c), thereby improving the adsorption efficiency. The elevated pHpzc value further confirms the influence of magnetic functionalization on the surface chemistry and adsorption performance of the MOBC.

3.2. Adsorption performance

The adsorption performances of OBC and MOBC for TC removal were evaluated under varying pH, adsorbent dosage, contact time, and temperature conditions. As shown in Fig. 4a, MOBC consistently outperformed OBC over the entire pH range (2–12), with optimal removal (>80%) observed at near-neutral pH (6–8). In comparison, the OBC achieved only ~40% removal under similar conditions. This difference is largely attributed to the surface charge behaviour. The pHpzc values of OBC and MOBC were 7.62 ± 0.6 and 8.68 ± 0.8, respectively, indicating that MOBC retains a positively charged surface over a broader pH range due to iron oxide incorporation. Because TC predominantly exists in a zwitterionic form at pH 6–8, MOBC facilitates enhanced electrostatic interactions, hydrogen bonding, and π–π stacking, leading to improved adsorption efficiency [2]. Fig. 4b reveals that increasing the adsorbent dosage enhanced the removal efficiency of both materials; however, MOBC consistently yielded higher removal rates, achieving >95% at 2.0 g/L, compared with ~60% for OBC. This improvement is associated with MOBC's larger surface area and the increased number of active sites due to magnetic modification. The kinetic analysis results shown in Fig. 4c shows that the MOBC reached near-equilibrium within 50–100 min, achieving ~98% removal, whereas the OBC plateaued at approximately 57% after 200 min. This indicates that MOBC not only adsorbs more efficiently, but also more rapidly, which is an advantage for real-time applications. Temperature-dependent experiments (Fig. 4d) demonstrated that the adsorption capacity of MOBC was highest at 25 °C and declined with increasing temperature, confirming the exothermic

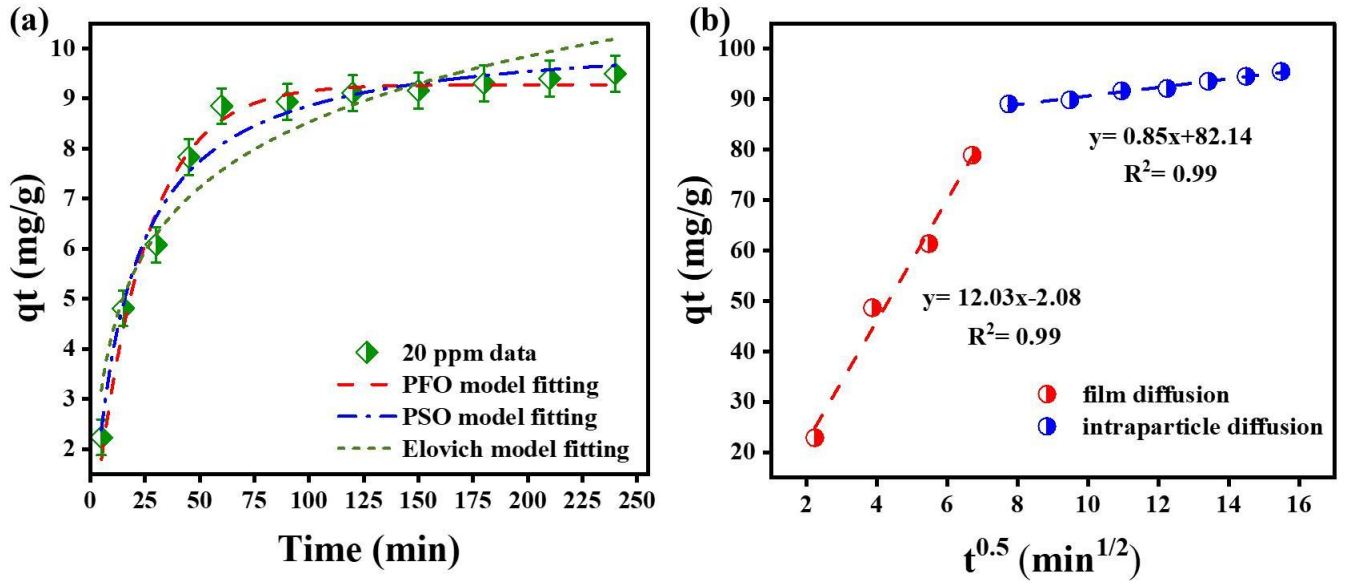

Figure 5. (a) Adsorption kinetics for TC on MOBC, (b) Intraparticle diffusion kinetics for adsorption of TC on MOBC (adsorption conditions: 20 mg/L TC, 2 g/L MOBC, 25 mL, pH = 6.04, 25 °C, 4h)

nature of the process. In contrast, the OBC exhibited a minimal response to temperature changes and consistently maintained lower removal rates.

Overall, MOBC displayed significantly superior adsorption behaviour under all tested conditions. These enhancements stem from improved physicochemical properties imparted by magnetic functionalization, such as increased porosity, higher surface area, and modified surface chemistry. These results highlight the potential of MOBC as a fast, efficient, and reusable adsorbent for tetracycline removal from contaminated water.

3.3. Adsorption kinetics

Kinetic modelling is indispensable for elucidating the adsorption mechanisms that govern the interactions between the adsorbents and target pollutants. Among the established kinetic models, the PFO, PSO, Elovich, and IPD models are widely employed due to their mechanistic interpretability across diverse adsorption systems [63–65]. In the present study, the adsorption kinetics of TC onto MOBC were investigated under optimized experimental conditions (TC = 20 mg/L, MOBC dosage = 2 g/L, pH = 6.04, and 25 °C) with contact times ranging from 0 to 240 min. Kinetic data were evaluated by fitting the four nonlinear models mentioned above (Fig. 5; Table 1, Table 2).

The PFO model, originally developed by Lagergren, assumes that the adsorption rate is proportional to the number of available active sites on the adsorbent surface. In this study, the PFO model provided the best fit (R^2 = 0.983; χ^2 = 0.107), indicating that the adsorption process is primarily governed by physisorption mechanisms, likely involving van der Waals forces or electrostatic interactions. The close agreement between the calculated and experimental equilibrium capacities further supported this interpretation.

Table 1. Kinetic parameters of TC adsorption on MOBC

Model Parameters		Unit	Initial TC concentration
			20 mg/L
PFO	q_e	mg/g	9.27 ± 0.13
	k_1	1/min	0.043 ± 0.003
	R^2	—	0.983
	X^2	—	0.107
PSO	q_e	mg/g	10.34 ± 0.22
	k_2	g/(mg·min)	0.006 ± 0.002
	R^2	—	0.979
	X^2	—	1.02
Elovich	α	g/(mg·min)	1.63 ± 0.67
	β	mg/g	0.52 ± 0.06
	R^2	—	0.918
	X^2	—	4.03

Comparable observations were reported by Ge et al. (2019) [63] for activated carbon and Houghton et al. (2025) [66] for fly ash-derived adsorbents, wherein the PFO model effectively captured the initial adsorption behaviour of TC.

Conversely, the PSO model, which is commonly associated with chemisorption involving valence forces or electron sharing, also exhibited a strong fit to the data (R^2 = 0.979). However, the slight deviations in the calculated equilibrium capacities suggest that chemisorption may act as a supplementary mechanism, particularly at extended contact times or elevated concentrations. This finding implies a dual-mechanism pathway: an initial rapid uptake dominated by physisorption followed by slower chemisorption processes.

Table 2. IPDM paramatters for TC adsorption on MOBC

Model	Stage	20 mg/L Paramaters		
		K_i	C_i	R^2
Intra-particle diffusion	I	12.03 ± 0.87	-2.08 ± 0.76	0.99
	II	0.85 ± 0.05	82.14 ± 4.45	0.99

Table 3. Isotherms parameters of TC adsorption on MOBC

Parameters		Unit	Solution temperature		
			25℃	45℃	65℃
Langmuir	Q_{max}	mg/g	240.21 ± 11.4	236.87 ± 16.4	222.23 ± 17.3
	$K_{LX}(10^{-3})$	L/mg	4.5 ± 0.04	1.88 ± 0.02	1.95 ± 0.023
	R^2	—	0.998	0.998	0.997
Freundlich	K_F	$(mg/g)\cdot(mg/L)^n$	4.81 ± 0.8	1.59 ± 0.3	1.52 ± 0.4
	n	—	0.6 ± 0.03	0.72 ± 0.03	0.70 ± 0.04
	R^2	—	0.988	0.993	0.988
Redlich-Peterson	K_{RP}	L/g	1.28 ± 0.024	0.49 ± 0.03	0.40 ± 0.02
	$a_{RP}x(10^{-5})$	$(mg/L)^{-g}$	1.63 ± 0.46	3.31 ± 0.55	1.65 ± 0.34
	g	—	0.84 ± 0.1	1.25 ± 0.008	1.70 ± 0.31
	R^2	—	0.998	0.998	0.998
Toth	qm	mg/g	447.26 ± 66.2	377.2 ± 23.75	240.21 ± 4.3
	$K_{TX}(10^{-3})$	L/mg	1.53 ± 0.08	1.65 ± 0.016	4.49 ± 0.004
	t	—	1.72 ± 0.28	1.26 ± 0.023	1.0 ± 0.13
	R^2	—	0.999	0.998	0.998
Sips	q_{ms}	mg/g	302.37 ± 58.0	267.17 ± 38.71	212.81 ± 31.06
	$K_{SX}(10^{-3})$	L/g	2.64 ± 0.11	2.16 ± 0.006	2.62 ± 0.78
	m	—	0.85 ± 0.08	1.03 ± 0.003	1.1 ± 0.09
	R^2	—	0.997	0.998	0.997

Similar multi-stage behaviours have been documented by Ghadim et al. (2013) [64] for graphene oxide and Hu et al. (2017) [67] for functionalized adsorbents.

The Elovich model, which is typically applicable to systems with highly heterogeneous surfaces, yielded the weakest correlation (R^2 = 0.918) and highest residual errors. These results imply that the MOBC surface exhibits a relatively uniform distribution of active sites, potentially due to the controlled synthesis conditions, including the dispersion of magnetic nanoparticles. Although the Elovich model has proven effective for describing complex adsorption kinetics in more heterogeneous systems [65,68] its limited applicability in this context further reinforces the homogeneity of the MOBC surface.

Taken together, the kinetic analysis suggested that the adsorption of TC onto MOBC was predominantly driven by physisorption, as evidenced by the superior fit of the PFO model.

The PSO model indicated a minor chemisorption component, whereas the poor performance of the Elovich model supported the hypothesis of a relatively homogeneous adsorbent surface.

To gain further insight into diffusion dynamics within the adsorbent matrix, an intraparticle diffusion model was also applied. The intraparticle diffusion plot of the MOBC adsorbent exhibited two distinct linear regions, indicating that the adsorption process occurred in multiple stages (Fig. 5b). In the first region, the high slope value (k_i=12.03) suggests that a rapid surface adsorption (film diffusion) takes place initially. The negative C_i value in this region implies that the boundary layer effect is negligible [69]. In the second region, the significantly lower slope (k_{ii}=0.85) reflects a slower diffusion process within the pores of the adsorbent, indicative that intraparticle diffusion contributes significantly as a rate-limiting mechanism, particularly in the later stages of adsorption, though it is not the sole controlling factor [70,71]. This aligns with the general understanding that, as adsorption progresses, the movement of the adsorbate into the pores of the adsorbent can slow down due to steric hindrance and decreased availability of binding sites, confirming the multi-stage nature of the adsorption mechanism [72,73]. Furthermore, the high positive intercept (C_i = 82.14) during this phase underscores the increasing influence of the boundary layer, which is consistent with other studies that explored layered adsorption mechanisms, where the boundary layer thickness increased as the adsorbate concentration diminished [62,74]. The high correlation coefficients (R^2 = 0.99) for both regions indicated an excellent fit of the model to the experimental data.

3.4. Adsorption isotherms

Adsorption isotherms are fundamental tools for elucidating the interaction mechanisms between an adsorbate and the adsorbent surface under equilibrium conditions. These models provide insights into the surface characteristics, adsorption capacity, energy distribution, and nature (homogeneous vs. heterogeneous) of adsorption sites. In the present study, the equilibrium adsorption behaviour of TC onto MOBC was comprehensively evaluated using five well-established non-linear isotherm models: Langmuir, Freundlich, Redlich–Peterson, Toth, and Sips (Fig. 6; Table 3). Experimental investigations were conducted at three different temperatures (25, 45, and 65 °C), allowing for an in-depth assessment of the thermodynamic and mechanistic aspects of the adsorption process.

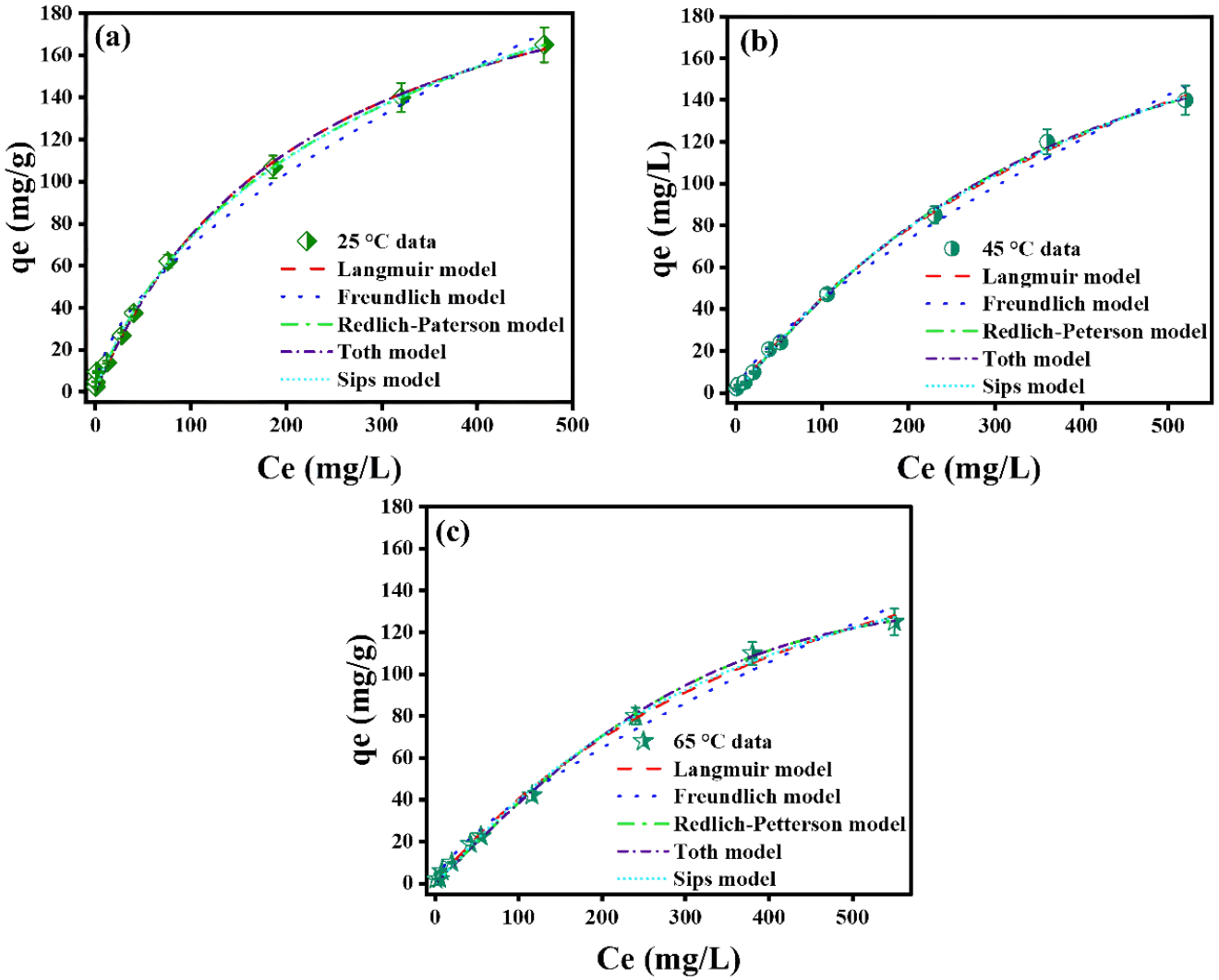

Figure 6. Isotherm models of TC adsorption at (a) 25 C, (b) 45 C, (c) 65 C (adsorption conditions: Initial TC concentration 5-800 mg/L, 2 g/L MOBC, 25 mL, pH = 6.04, 2h)

The Langmuir isotherm model, which is based on the assumption of monolayer adsorption onto a surface with a finite number of identical and energetically equivalent adsorption sites, exhibited the highest correlation coefficients across all temperatures (R^2 = 0.997–0.998). This excellent fit implies that the MOBC surface behaves in a relatively homogeneous manner, and that the adsorption process reaches saturation when each adsorption site is occupied by a single TC molecule. The Langmuir maximum adsorption capacity was highest at 25 °C (240.21 mg/g), with a slight decrease at elevated temperatures (222.23 mg/g at 65 °C). This inverse relationship between temperature suggests an exothermic adsorption process, further reinforcing the dominance of physisorption mechanisms such as electrostatic interactions, hydrogen bonding, and π–π interactions [75].

The Freundlich model, which assumes a heterogeneous surface with sites of varying adsorption energies and allows for multilayer formation, yielded comparatively lower correlation coefficients (R^2 = 0.988–0.993) and n values less than 1. These n values, a measure of adsorption intensity, indicate less favourable adsorption and surface heterogeneity. The inadequacy of this model to fully capture the adsorption behaviour suggests that multilayer formation and significant energetic heterogeneity are not predominant in the TC–MOBC system [76].

The Redlich–Peterson model, a hybrid isotherm combining elements of both Langmuir and Freundlich equations, provided an excellent fit to the experimental data (R^2 ≈ 0.998). The heterogeneity parameter g approached unity across all tested conditions, indicating that the model was effectively reduced to the Langmuir form. This convergence supports the conclusion that the surface is relatively homogeneous, and monolayer adsorption is the dominant mechanism [77].

Similarly, the Toth and Sips models, both extensions of the Langmuir model designed to accommodate surface heterogeneity, also produced near-perfect correlations (R^2 ≈ 0.998–0.999). Importantly, the t and m parameters, which quantify the deviation from ideal homogeneity, were close to 1, suggesting only minor surface heterogeneity and further confirming the pseudo-homogeneous nature of the MOBC.

Table 4. Thermodynamic parameters of the adsorption process of TC by MOBC

ΔH°(kj/mol)	ΔS° (J/mol K)	ΔG° (kj/mol)		
		298 K	313 K	328 K
-3.74	47.25	-17.83	-18.77	-19.70

These findings imply that, while some variability in adsorption energy exists, it is minimal and does not significantly impact the overall adsorption mechanism [78,79].

Taken together, the isotherm analysis clearly identified the Langmuir model as the most appropriate representation of the adsorption process, supporting the concept of monolayer adsorption onto a surface with relatively uniform energy sites. The high performance of the Redlich–Peterson, Toth, and Sips models corroborates this conclusion, indicating that the MOBC surface possesses quasi-homogeneous characteristics.

In contrast, the relatively poor performance of the Freundlich model effectively rules out multilayer adsorption or highly heterogeneous surface interactions.

From a materials science perspective, the magnetic functionalization of biochar not only increases its surface area but also appears to enhance the surface uniformity and accessibility of adsorption sites. This leads to more consistent interactions between the TC molecules and the MOBC surface, enabling more efficient and predictable adsorption. The dominance of physisorption also implies that desorption or regeneration of the adsorbent can be achieved under mild conditions, further supporting the practical applicability of MOBC in water treatment and pharmaceutical contaminant removal.

3.5. Adsorption thermodynamics of TC

To clarify the adsorption mechanism and spontaneity of TC uptake by MOBC, the key thermodynamic parameters were evaluated. These included standard enthalpy (ΔH°), entropy (ΔS°), and Gibbs free energy (ΔG°), calculated using the van't Hoff equation (Table 4). The negative ΔH° value (-3.74 kJ/mol) confirms an exothermic process, suggesting that physisorption is dominated by van der Waals forces, hydrogen bonding, and electrostatic interactions [80,81]. The positive ΔS° (+47.25 J/mol·K) indicates increased disorder at the solid–liquid interface, likely due to desolvation effects and structural rearrangements [82]. ΔG° values were consistently negative across 298–338 K (−17.83 to −19.70 kJ/mol), confirming the spontaneous nature of adsorption [83]. Moreover, the increasingly negative ΔG° at higher temperatures reflects enhanced thermodynamic favourability, primarily owing to entropic contributions [84]. Overall, the data suggest that TC adsorption onto MOBC is spontaneous, exothermic, and entropy-driven, which is consistent with physical adsorption mechanisms and supports its potential in sustainable water treatment applications.

Table 5. The adsorption capacity of TC on the MOBC adsorbent in the different water samples (n=3)

Sample	Spiked, mg/L	Found, mg/g
Distilled water	10	4.75 ± 1
	20	9.5 ± 1
Drinking Water	10	4.6 ± 2
	20	9.32 ± 1
Tap Water	10	4.42 ± 1
	20	9.27 ± 2
Waste Water	10	4.25 ± 1
	20	9.17 ± 2

(adsorption conditions: 10-20 mg/L TC, 2 g/L MOBC, 25 mL, pH = 6.04, 2h)

3.6. Desorption/ recycling and real sample application

Desorption and reusability are critical for evaluating the practical applicability of MOBC. Various eluents—ACN, HCl, NaOH, methanol, and ethanol—were tested, and NaOH exhibited the highest desorption efficiency (87%), as shown in **Supplementary** Table S1. This high desorption rate suggests that TC adsorption occurs mainly via weak van der Waals forces, in agreement with isotherm and thermodynamic findings.

Reusability tests over four adsorption–desorption cycles (Fig. S2) showed a gradual decrease in performance, with approximately 50% removal efficiency maintained by the fourth cycle. The method's reliability was confirmed using real water samples (distilled water, drinking water, tap water, and wastewater) spiked with TC at two concentrations. As presented in Table 5, the adsorption capacities in real matrices were comparable to that in distilled water, demonstrating MOBC effectiveness in complex environments.

Adsorption studies conducted on real water samples revealed that the MOBC adsorbent exhibited high performance for tetracycline removal at a fixed dose of 2 g/L. Tetracycline was added to all samples at initial concentrations of 10 mg/L and 20 mg/L, and the adsorption capacity was calculated. In the distilled water sample, qe values of 4.75 mg/g and 9.5 mg/g were obtained, respectively. These values were recorded as 4.6 ± 2 mg/g and 9.32 ± 1 mg/g in drinking water, and 4.42 ± 1 mg/g and 9.27 ± 2 mg/g in tap water. In the wastewater sample, it was observed that it maintained its high performance even in complex matrix conditions with values of 4.25 ± 1 mg/g and 9.17 ± 2 mg/g. The obtained data showed that MOBC is an effective tetracycline remover that exhibits an adsorption capacity close to that of distilled water, even in matrices containing ionic components. This finding supports the potential for the broad use of MOBC in environmental applications.

4. Conclusion

This study demonstrated the effective transformation of olive pomace into a functional adsorbent material through magnetic modification for the removal of tetracycline from aqueous environments. MOBC showed significantly enhanced adsorption capacity and kinetics compared to OBC, attributed to its increased surface area, pore structure, and surface functional groups. Adsorption experiments indicated that the process was best described by the Langmuir isotherm and pseudo-first-order kinetic models, with thermodynamic data confirming a spontaneous and exothermic mechanism predominantly governed by physisorption. The high desorption efficiency and consistent performance in real water samples further underscores the practical applicability of MOBC. These findings suggest that MOBC is a promising and environment-friendly adsorbent for the removal of pharmaceutical pollutants, contributing to the advancement of sustainable wastewater treatment strategies.

Acknowledgment

This study was carried out at Burdur Mehmet Akif Ersoy University, Faculty of Arts and Science, Chemistry Department. I am grateful to Prof. Dr. Erdal Kendüzler for their support.

References

[1] X. Zhang, D. Zhen, F. Liu, R. Chen, Q. Peng, Z. Wang, An achieved strategy for magnetic biochar for removal of tetracyclines and fluoroquinolones: Adsorption and mechanism studies, Bioresour Technol, 369, 2023, 128440.

[2] B. Kabak, Synthesis and application of Tb-MOF for efficient fluorescence detection and removal of tetracycline from aqueous environments, J Mol Struct, 1322, 2025, 140348.

[3] Y. Amangelsin, Y. Semenova, M. Dadar, M. Aljofan, G. Bjørklund, The impact of tetracycline pollution on the aquatic environment and removal strategies, Antibiotics, 12, 2023, 440.

[4] N.T. Huong, H.T. Huyen, T.Q. Phong, Conjugation of tetracycline with carrier proteins and production of its polyclonal antibody for the development of rapid test, Vietnam J Sci Technol, 62 (1), 2024, 23-34.

[5] J. Jaroszewski, N. Mamun, K. Czaja, Bidirectional interaction between tetracyclines and gut microbiome, Antibiotics, 12, 2023, 1438.

[6] J. Wang, P. Li, Y. Zhao, X. Zeng, Nb/N Co-Doped layered perovskite Sr_2TiO_4: preparation and enhanced photocatalytic degradation tetracycline under visible light, Int. J. Mol. Sci. 2022, 23, 10927.

[7] L. Qian, B. Chen, Dual role of biochars as adsorbents for aluminum: The effects of oxygen-containing organic components and the scattering of silicate particles, Environ. Sci. Technol, 47(15), 2013, 8759-8768.

[8] S. Wang, H. Zhao, J. Liu, X. Wang, J. Li, E. Shi, C. Wang, J. Yang, Z. Zhang, A study on and adsorption mechanism of ammonium nitrogen by modified corn straw biochar, R Soc Open Sci, 10, 2023, 221535.

[9] P. He, Q. Yu, H. Zhang, L. Shao, F. Lü, Removal of Copper (II) by biochar mediated by dissolved organic matter, Sci, Rep, 7, 2017, 7091.

[10] L. Qian, B. Chen, Interactions of aluminum with biochars and oxidized biochars: Implications for the biochar aging process, J Agric Food Chem, 61(36), 2013, 8174-8181.

[11] X. Zhang, J. Hou, T. Cai, S. Zhang, L. Shen, Q. Zhang, Functionalized construction of highly aromatic condensed graphitized biochar for tetracycline adsorption, Environ Technol Innov, 37, 2025, 104002.

[12] L. Lin, L. Ning, S. Chen, B. Wang, H. Zhuang, X. Jing, Q. Li, Ultra-large adsorption capacity for tetracycline by defatted Schizochytrium limacinum residue biochar, Algal Res, 88, 2025, 104011.

[13] G. Loebsack, K.K.C. Yeung, F. Berruti, N.B. Klinghoffer, Impact of biochar physical properties on adsorption mechanisms for removal of aromatic aqueous contaminants in water. Biomass Bioenergy 194, 2025, 107617.

[14] A. Bano, B. Prasad, H. Dave, K.S. Prasad, A mechanistic insight on non-steroidal anti-inflammatory drug, ketoprofen removal from pharmaceutical wastewater by a magnetic biochar: Batch and fixed bed adsorption studies, Inorg Chem Commun, 173, 2025, 113802.

[15] A. Durán, J.M. Monteagudo, J. Delgado, Degradation of antipyrine in water with activated persulfate aided with biochar of olive pomace, J Environ Manage, 368, 2024, 122159.

[16] I, Rabichi, K, Ezzahi, F.E. Yaacoubi, Z. Izghri, K. Ennaciri, A. Ounas, A. Yaacoubi, A. Baçaoui, M. Hafidi, L. El Fels, Evaluating the fixed-bed column adsorption capacity of olive pomace biochar activated with KOH and H_3PO_4 for olive mill wastewater treatment: Insights from TOC and HPLC analysis. Chemosphere, 377, 2025, 144356.

[17] L.M. Ruiz, M. Fernández, A. Genaro, J. Martín-Pascual, M. Zamorano, Multi-parametric analysis based on physico-chemical characterization and biochemical methane potential estimation for the selection of industrial wastes as co-substrates in anaerobic digestion, Energies 16, 2023, 5444.

[18] C. Nasopoulou, K. Lytoudi, I. Zabetakis, Evaluation of olive pomace in the production of novel broilers with enhanced in vitro antithrombotic properties, Eur J Lipid Sci Technol, 120(4), 2018, 1700290.

[19] A. Ncube, G. Fiorentino, C. Panfilo, M. De Falco, S. Ulgiati, Circular economy paths in the olive oil industry: a Life Cycle Assessment look into environmental performance and benefits, Int J Life Cycle Assess, 29, 2024, 1541–1561.

[20] C. Romero, E. Medina, M. A. Mateo, M. Brenes, New by-products rich in bioactive substances from the olive oil mill processing, J Sci Food Agric, 98, 2018, 225–230.

[21] N. Montegiove, A.M. Gambelli, E. Calzoni, A. Bertoldi, D. Puglia, C. Zadra, C. Emiliani, G. Gigliotti, Biogas production with residuals deriving from olive mill wastewater and olive pomacewastes: quantification of produced energy, spent energy, and process efficiency, Agronomy 14, 2024, 531.

[22] J.D. Palmeira, D. Araújo, C.C. Mota, R.C. Alves, M.B.P.P. Oliveira, H.M.N. Ferreira, Fermentation as a strategy to valorize olive pomace, a by-product of the olive oil industry, Fermentation, 9, 2023, 442.

[23] M. Puig-Gamero, J.R. Trapero, P. Sánchez, L. Sanchez- Silva, Is methanol synthesis from co-gasification of olive pomace and petcoke economically feasible?, Fuel, 278, 2020, 118284.

[24] G. Espadas-Aldana, P. Guaygua-Amaguaña, C. Vialle, J.-P. Belaud, P. Evon, C. Sablayrolles, Life cycle assessment of olive pomace as a reinforcement in polypropylene and polyethylene biocomposite materials: A new perspective for the valorization of this agricultural by-product, Coatings, 11, 2021, 525.

[25] M. Centrone, M. D'Agostino, G. Difonzo, A. De Bruno, A. Di Mise, M. Ranieri, C. Montemurro, G. Valenti, M. Poiana, F. Caponio, G. Tamma, Antioxidant efficacy of olive by-product extracts in human Colon HCT8 Cells, Foods, 10, 2021,11.

[26] D.L.C. Rodrigues, A.C.F.P. Fuhr, J.A. Guido, C.F. de Azevedo, A.M. Rangel, G.L. Dotto, S.Y. Alomar, F.M. Machado, Olive biomass-derived magnetic activated biochar for ciprofloxacin removal: Integrated kinetic, isotherm, thermodynamic, and spectroscopic analysis. Sep Purif Technol, 360, 2025, 131014.

[27] T.M. Huggins, A. Haeger, J.C. Biffinger, Z.J. Ren, Granular biochar compared with activated carbon for wastewater treatment and resource recovery, Water Res, 94, 2016, 225-232.

[28] E. Gul, K.A.B. Alrawashdeh, O. Masek, Ø. Skreiberg, A. Corona, M. Zampilli, L. Wang, P. Samaras, Q. Yang, H. Zhou, P. Bartocci, F. Fantozzi, Production and use of biochar from lignin and lignin-rich residues (such as digestate and olive stones) for wastewater treatment, J Anal Appl Pyrolysis, 158, 2021, 105263.

[29] A. Hmid, D. Mondelli, S. Fiore, F.P. Fanizzi, Z. Al Chami, S. Dumontet, Production and characterization of biochar from three-phase olive mill waste through slow pyrolysis, Biomass & Bioenergy, 71, 2014, 330e339.

[30] N.S. Hassan, A.A. Jalil, N.M. Izzuddin, M.B. Bahari, A.H. Hatta, R.M. Kasmani, N. Norazahar, Recent advances in lignocellulosic biomass-derived biochar-based photocatalyst for wastewater remediation, J Taiwan Inst Chem Eng, 163, 2024, 105670.

[31] G. Peer, H. Azaizeh, E. Kurzbaum, B. Shahar, N. Mattar, S.P. Azerra, Valorization of olive mill solid waste-derived biochar: An efficient approach for simultaneous adsorption and oxidation of micropollutant in surface water, J Water Process Eng, 56, 2023, 104461.

[32] S. Nand, P.P. Singh, S. Verma, S. Mishra, A. Patel, S. Shukla, Pankaj Kumar Srivastava, Biochar for mitigating pharmaceutical pollution in wastewater: A sustainable solution, Sci Total Environ, 966, 2025, 178743.

[33] O. Bayram, E. Köksal, E. Moral, F. Göde, E. Pehlivan, Efficient decolorization of cationic dye (malachite green) by natural-based biosorbent (nanomagnetic Sophora Japonica fruit seed biochar), J Disper Sci Technol, 45, 2022, 117-128.

[34] O. Bayram, E. Moral, E. Köksal, F. Göde, E. Pehlivan, Removal of methyl blue and malachite green from water using biodegradable magnetic Tamarindus Indica fruit seed biochar: Characterization, equilibrium study, modelling and thermodynamics, SCENV, 3, 2023, 100023.

[35] S. Mortazavian, S.E.H. Murph, J. Moon, Biochar nanocomposite as an inexpensive and highly efficient carbonaceous adsorbent for hexavalent chromium removal, Materials 15, 2022, 6055.

[36] P. Sun, C. Hui, R.A. Khan, J. Du, Q. Zhang, Y.H. Zhao, Efficient removal of crystal violet using Fe_3O_4-coated biochar: The role of the Fe_3O_4 nanoparticles and modeling study of their adsorption behavior, Sci Rep, 5, 2025, 12638.

[37] N.A. Guel-Nájar, J.C. Rios-Hurtado, E.M. Muzquiz-Ramos, G.I. Dávila-Pulido, A.A. González-Ibarra, A.M. Pat-Espadas, Magnetic biochar obtained by chemical coprecipitation and pyrolysis of corn cob residues: Characterization and methylene blue adsorption, Materials, 16, 2023, 3127.

[38] C. Lomenech, Ch. Hurel, L. Messina, M. Schembri, P. Tosi, F. Orange, F. Georgi, A. Mija & P. Kuzhir, A humins-derived magnetic biochar for water purification by adsorption and magnetic separation, Waste Biomass Valori, 12, 2021, 6497–6512.

[39] P.B. Hassan, R.O. Rasheed, K. Zargoosh, Cadmium and lead removal from aqueous solution using magnetite nanoparticles biofabricated from Portulaca oleracea leaf extract, J Nanomater, 2022(1), 2022, 1024554.

[40] A. Azizi, Green synthesis of Fe_3O_4 nanoparticles and its application in preparation of Fe_3O_4/cellulose magnetic nanocomposite: A suitable proposal for drug delivery systems, J Inorg Organomet P, 30, 2020, 3552–3561.

[41] F. Ghasemy-Piranloo, F. Bavarsiha, S. Dadashian, Tribological properties of core/shell Fe_3O_4/TiO_2 composites as additives in base oil, J Sol-Gel Sci Technol, 103, 2022, 908–920.

[42] D. Devanand, R. Khatkar, S. Nahar, S. Nagpal, Remediation of chlorpyrifos by utilizing waste packaging wood as magnetic biochar, Remediation, 34, 2024, e21781.

[43] Y. Gu, Y. Xue, D. Zhang, Adsorption of aniline by magnetic biochar with high magnetic separation efficiency, Environ Pollut Bioavailab, 33 (1), 2021, 66–75.

[44] T. Ao, P. Kalita, C. Blada, N.P. Brown, K. Fulford, P. Gard, M. Geissel, H. Hanshaw, M. Montoya, S. Payne, E. Scoglietti, A. Smith, C.S. Speas, J.L. Porter, C.T. Seagle, Exploring the high-pressure phases of carbon through X-ray diffraction of dynamic compression experiments on Sandia's Z pulsed power facility, Minerals 13, 2023, 1203.

[45] X. Liu, R. Han, X. Zhao, D. Ma, R. Han, Characterization of bio-char from pyrolysis of wheat straw and its evaluation on methylene blue adsorption, Desalin Water Treat, 40, 2012, 1–7.

[46] N. Strutynska, I. Zatovsky, N. Slobodyanik, A. Malyshenko, Y. Prylutskyy, O. Prymak, I. Vorona, S. Ishchenko, N. Baran, A. Byeda, A. Mischanchuk, Preparation, characterization, and thermal transformation of poorly crystalline sodium- and carbonate-substituted calcium phosphate, Eur J Inorg Chem, 2015 (4), 2015, 622–629.

[47] Y. Zhang, X. Kang, J. Tan, R.L. Frost, Influence of calcination and acidification on structural characterization of Anyang anthracites, Energy Fuel, 27 (11), 2013,7191–7197.

[48] S.A.M. Zobir, S. Abu Bakar, S. Abdullah, Z. Zainal, S.H. Sarijo, M. Rusop, Raman spectroscopic study of carbon nanotubes prepared using Fe/ZnO–palm olein–chemical vapour deposition, J Nanomater, 2012(1), 2012, 451473.

[49] K. Kisu, E. Iwama, W. Naoi, P. Simon, K. Naoi, Electrochemical kinetics of nanostructure $LiFePO_4$/graphitic carbon electrodes, Electrochem Commun, 72, 2016, 10–14.

[50] V. Roungos, C.G. Aneziris, H. Berek, Novel Al_2O_3-C refractories with less residual carbon due to nanoscaled additives for continuous steel casting applications, Adv Eng Mater, 14 (4), 2012, 255–261.

[51] I.W. Suryawan, I.Y. Septiariva, E.N. Fauziah, B.S. Ramadan, F.D. Qonitan, N.L. Zahra, A. Sarwono, M.M. Sari, K.K. Ummatin, L.J. Wei, Municipal solid waste to energy: Palletization of paper and garden waste into refuse derived fuel, J Ecol Eng, 23 (4), 2022, 64–74.

[52] D. Aller, S. Bakshi, D.A. Laird, Modified method for proximate analysis of biochars, J Anal Appl Pyrol, 124, 2017, 335–342.

[53] Z. Shen, Y. Zhang, F. Jin, D.S. Alessi, Y. Zhang, F. Wang, O. McMillan, A. Al-Tabbaa, Comparison of nickel adsorption on biochars produced from mixed softwood and Miscanthus straw, Environ Sci Pollut Res, 25, 2018, 14626–14635.

[54] M.K. Rafiq, R.T. Bachmann, M.T. Rafiq, Z. Shang, S. Joseph, R. Long, Influence of pyrolysis temperature on physico-chemical properties of corn stover (*Zea mays* L.) biochar and feasibility for carbon capture and energy balance, PLoS ONE, 11 (6), 2016, e0156894.

[55] Y. Chen, L. Li, Q. Wen, R. Yang, Y. Zhao, X. Rao, J. Li, S. Xu, H. Song, Oxidative magnetic modification of pristine biochar assisted by ball-milling for removal of methylene blue and tetracycline in aqueous solution, Sustainability, 14, 2022, 9349.

[56] M. Idrees, S. Jeelani, V.K. Rangari, 3D printed sustainable biochar-recycled PET composite, ACS Sustain Chem Eng, 6 (10), 2018, 12331–12339.

[57] X. Zhang, X. Yang, X. Yuan, S. Tian, X. Wang, H. Zhang, L. Han, Effect of pyrolysis temperature on composition, carbon fraction and abiotic stability of straw biochars: correlation and quantitative analysis, Carbon Res, 1, 2022, 17.

[58] E.E. Oprescu, E.C. Enascuta, G. Vasilievici, N.D. Banu, I. Banu, Preparation of magnetic biochar for nitrate removal from aqueous solutions, React Kinet Mech Catal, 135, 2022, 2629–2642.

[59] J.M. Monteagudo, A. Duŕan, M. Alonso, A.-I. Stoica, Investigation of effectiveness of KOH-activated olive pomace biochar for efficient direct air capture of CO_2, Sep Purif Technol, 352, 2025, 127997.
[60] A. Alcazar-Ruiz, S. Maisano, V. Chiodo, F. Urbani, F. Dorado, L. Sanchez-Silva, Enhancing CO_2 capture performance through activation of olive pomace biochar: A comparative study of physical and chemical methods, SM&T, 42, 2024, e01177.
[61] M. Thommes, K. Kaneko, A.V. Neimark, J.P. Olivier, F. Rodriguez-Reinoso, J. Rouquerol, K.S.W. Sing, Physisorption of gases, with special reference to the evaluation of surface area and pore size distribution (IUPAC Technical Report), Pure Appl Chem, 87 (9–10), 2015, 1051–1069.
[62] R, Şensoy, B, Kabak, E, Kendüzler, Kinetic and isothermal studies of naproxen adsorption from aqueous solutions using walnut shell biochar, React Kinet Mech Catal, 137, 2024, 1031–1049.
[63] Y. Ge, B. Cheng, X. Wang, T. Zhao, Rapid preparation of activated carbon fiber felt under microwaves: Pore structures, adsorption of tetracycline in water, and mechanism, Ind Eng Chem Res, 59 (1), 2020, 146–153.
[64] E.E. Ghadim, F. Manouchehri, G. Soleimani, H. Hosseini, S. Kimiagar, S. Nafisi, Adsorption properties of tetracycline onto graphene oxide: Equilibrium, kinetic and thermodynamic studies, Plos One, 8(11), 2013, e79254.
[65] J. Hoslett, H. Ghazal, E. Katsou, H. Jouhara, The removal of tetracycline from water using biochar produced from agricultural discarded material, Sci Total Environ, 751, 2021, 141755.
[66] E.E. Houghton, L. Yapi, N. Haneklaus, H.G. Brink, S.M. Tichapondwa, Coal fly ash-based adsorbents for tetracycline removal: Comparative insights into modification and zeolite conversion, J Xenobiot, 15, 2025, 36.
[67] X. Hu, Y. Zhao, H. Wang, X. Tan, Y. Yang, Y. Liu, Efficient removal of tetracycline from aqueous media with a Fe_3O_4 Nanoparticles@graphene oxide nanosheets assembly, Int J Environ Res Public Health, 14, 2017, 1495.
[68] E.M. Denesa, T. Laysandra, F.E. Soetaredjo, W. Irawaty, S. Ismadji, J.N. Putro, S.P. Santoso, Binary adsorption kinetics of tetracycline and doxycycline on HKUST-1: Modification pseudo first and second order models, Eng Chem, 8, 2024, 31-40.
[69] M. Andrunik, T. Bajda, Removal of pesticides from waters by adsorption: Comparison between synthetic zeolites and mesoporous silica materials. A review, Materials, 14, 2021, 3532.
[70] N. Basereh, S. Wainaina, A. Mahboubi, M.J. Taherzadeh, Fractionation of waste-derived volatile fatty acids by multi-stage adsorption using activated charcoal and Diaion HP-20 resin, Bioengineered, 16 (1), 2025, 2458366.
[71] S. Vasudevan, J. Lakshmi, G. Sozhan, Studies relating to removal of arsenate by electrochemical coagulation: Optimization, kinetics, coagulant characterization, Sep Sci Technol, 45 (9), 2010, 1313–1325.
[72] S.M. Yusuff, O.K. Khim, W.M.Z.W. Yunus, A. Fitrianto, M.B. Ahmad, Adsorption kinetics and isotherm of methylene blue by thermally treated alum-based water treatment plant sludge, Int J Adv Appl Sci, 4 (12), 2017, 89–93.
[73] W. An, Y. Liu, H. Chen, X. Sun, Q. Wang, X. Hu, J. Di, Adsorption properties of Pb(II) and Cd(II) in acid mine drainage by oyster shell loaded lignite composite in different morphologies, Scientific Reports 14, 2024, 11627.
[74] L. Natrayan, S. Kaliappan, C.N.D.K. Reddy, M. Karthick, N.S. Sivakumar, P.P Patil, S. Sekar, S. Thanappan, Development and characterization of carbon-based adsorbents derived from agricultural wastes and their effectiveness in adsorption of heavy metals in wastewater, Bioinorg Chem 2022 (1), 2022, 1659855.
[75] B. Alawa, S. Singh, S. Chakma, R. Kishor, C.S. Lundborg, Vishal Diwan, Development of novel biochar adsorbent using agricultural waste biomass for enhanced removal of ciprofloxacin from water: Insights into the isotherm, kinetics, and thermodynamic analysis, Chemosphere 375, 2025, 144252.
[76] C. Zhang, Y. Lei, J. Qian, Y. Qiao, J. Liu, S. Li, L. Dai, K. Sun, H. Guo, G. Sui, W. Jing, Sorption of organochlorine pesticides on polyethylene microplastics in soil suspension, Ecotoxicol Environ Saf, 223, 2021, 112591.
[77] M.A. Al-Ghouti, D.A. Da'ana, Guidelines for the use and interpretation of adsorption isotherm models: A review, J Hazard Mater, 393, 2020, 122383.
[78] J.Y.J. Yeo, M. Bergaoui, A. Nakhli, D.S. Khaerudini, F.E. Soetaredjo, S. Ismadji, J. Sunarso, N.M. Al-Hada, B.A. Al-Asbahi, M. Khalfaoui, Exploring interface interactions in antibiotics adsorption on bentonite-alginate composite: Insights from advanced simulations and adsorption isotherms modelling, Surf Interface, 60, 2025, 106038.
[79] D.D.A. Grefa, J.E. Guevara Sánchez, L.R. Bravo Sánchez, M.S. Pomares Alfonso, M.E.V. Tagle, Rice husk ash as sorbent for solid phase extraction of diclofenac, ibuprofen and carboplatin residues from waters, Microchem J, 195, 2023, 109361.
[80] X. Hu, X. Du, Adsorption of tea polyphenols using microporous starch: A study of kinetics, equilibrium and thermodynamics, Molecules, 24, 2019, 1449.
[81] R. Üzek, S. Şenel, A. Denizli, Investigation of thermodynamic, kinetic, and isothermal parameters for the selective adsorption of bisphenol A, ACS Omega, 7 (22), 2022, 18940–18952.
[82] E.R.A. Singam, Y. Zhang, G. Magnin, I. Miranda-Carvajal, L. Coates, R. Thakkar, H. Poblete, J. Comer, Thermodynamics of adsorption on graphenic surfaces from aqueous solution, Chem Theory Comput, 15 (2), 2019, 1302–1316.
[83] Z. Zhang, X. Jin, H. Chen, X. Zhang, C. Tan, X. Bai, Y. Gong, Surfactant-modified construction waste bricks for the removal of diclofenac from aqueous solutions, Appl Sci, 13, 2023, 6306.
[84] L. Kong, M. Zhang, Adsorption of methylene blue on chestnut shell-based activated carbon: Calculation of thermodynamic parameters for solid–liquid interface adsorption, Catalysts, 12, 2022, 813.

Supplementary

Section 1

Adsorption Kinetics and Isotherms models equations

Pseudo-first-order kinetic model (Lagergren model):

The rate of adsorption was assumed to be directly proportional to the number of unoccupied sites.

$$q_t = q_e\left(1 - e^{-k_1 t}\right) \quad (1)$$

k_1 (1/min) constant rate of pseudo-first order
q_e (mg/g) theoretical value of the adsorption capacity

Pseudo-second-order kinetic model:

This is based on the assumption that the rate-limiting step is chemisorption involving valence forces.

$$q_t = \frac{q_e^2 k_2 t}{1 + q_e k_2 t} \quad (2)$$

k_2 (g/(mg.min) constant rate of pseudo-second order
q_e (mg/g) theoretical value of the adsorption capacity

Elovich model:

It is applicable to heterogeneous surfaces and is often used in chemisorption.

$$q_t = \frac{1}{\beta} ln(1 + \alpha\beta t) \quad (3)$$

α (mg/g·min) is the initial rate constant;
β (mg/g) is Elovich constant.

Intraparticle diffusion model (Weber–Morris model):

Assess whether intraparticle diffusion is the sole or multiple rate-limiting step.

$$q_t = k_{int} t^{0.5} + C \quad (4)$$

k_{int} (mg/g.min$^{1/2}$) the rate constant for intra-particle diffusion,
C signifies the boundary layer thickness.

Each kinetic model was fitted to the experimental data using nonlinear regression methods and the best-fit model was selected based on the correlation coefficient (R^2) values.

Langmuir isotherm model:

Assumes monolayer adsorption onto a surface with a finite number of identical sites.

$$q_e = \frac{q_m K_L C_e}{1 + K_L C_e} \quad (5)$$

qm (mg/g) maximum adsorption capacity;
K_L (L/mg) Langmuir constant.

Freundlich isotherm model:

An empirical model describing adsorption on heterogeneous surfaces.

$$q_e = K_F C_e^n \quad (6)$$

K_F (mg/g)·(L/mg)^n Freundlich constant;
n Freundlich intensity parameter.

Redlich–Peterson isotherm model:

A hybrid isotherm incorporating both Langmuir and Freundlich characteristics.

$$q_e = \frac{K_{RP} C_e}{1 + a_{RP} C_e^g} \quad (8)$$

K_{RP} (L/g) and a_{RP} (mg/L)-g Redlich–Peterson constant
g heterogeneity factor.

Toth isotherm model:

The Toth isotherm model is an empirical extension of the Langmuir equation, which is designed to account for surface heterogeneity and to better fit the experimental data at higher adsorbate concentrations.

$$q_e = \frac{q_m K_T C_e}{(1 + (K_T C_e)^t)^{1/t}} \quad (9)$$

where qT, KT, and t represent the Toth maximum adsorption capacity (mg g-1), Toth equilibrium constant (L mg-1), and the dimensionless index of the system heterogeneity, respectively. The value of t is constrained at ≤1 in the fitting, where the system is considered as heterogeneity if t <1, otherwise Langmuir model is recovered if t =1

Sips isotherm model:

Combines the features of the Langmuir and Freundlich isotherms, useful for heterogeneous systems at high concentrations.

$$q_e = \frac{q_m (K_S C_e)^m}{1 + (K_S C_e)^m} \quad (10)$$

qm (mg/g) maximum adsorption capacity;
K_S (L/g) Sips isotherm constant; m heterogeneity factor

The isotherm parameters were determined by nonlinear regression using the experimental equilibrium data. The suitability of each model was evaluated based on the regression coefficients and error analysis metrics.

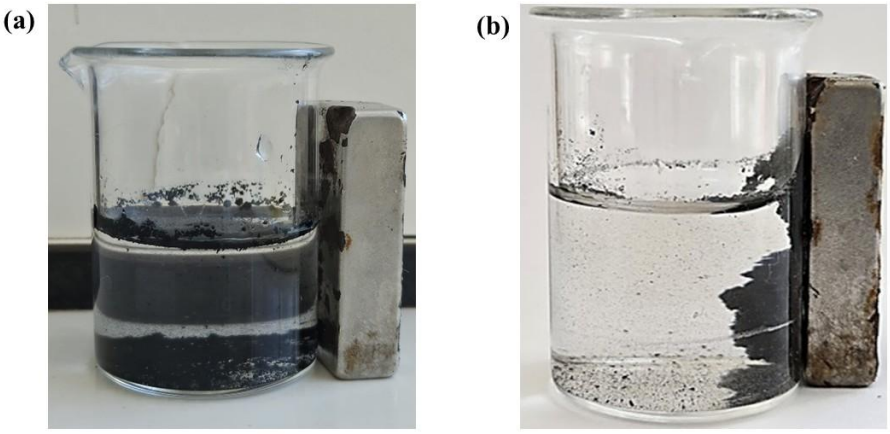

Figure S1. Images of (a) biochar (OBC) and (b) magnetic biochar (MOBC) samples

Table S1. Desorption efficiency (%) of TC from the MOBC

Desorption agents	Desorption efficiency (%)
ACN	—
Methanol	10 ± 3
Ethanol	20 ± 2
0.5 M HCl	12 ± 2
0.5 M NaOH	50 ± 3
1 M NaOH	57 ± 2
1.5 M NaOH	75 ± 4
2 M NaOH	87 ± 3

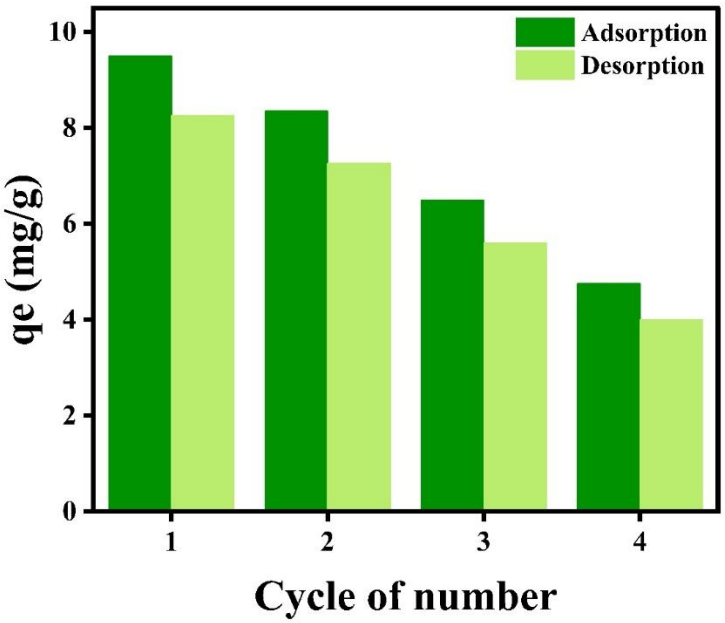

Figure S2. TC adsorption–desorption cycle on MOBC